

# Defect detection in 3D printed carbon fibre composites using X-ray Computed Tomography

Jeroen Soete<sup>1</sup>, Brice Badoux<sup>1</sup>, Yentl Swolfs<sup>1</sup>, Larissa Gorbatikh<sup>1</sup>, Martine Wevers<sup>1</sup>

<sup>1</sup>Materials Engineering (MTM) KU Leuven, Kasteelpark Arenberg 44, box 2450, 3001 Leuven, Belgium,

e-mail: [jeroen.soete@kuleuven.be](mailto:jeroen.soete@kuleuven.be)

## Abstract

X-ray Computed Tomography (X-ray CT) has become a vital tool for product quality inspection. The X-ray CT analysis of 3D printed composites, with a layer-by-layer structure of carbon fibre/polyamide and polyamide plies, demonstrates how the void content increases with an increasing number of consecutive carbon fibre layers. Not only the void content, but also the pore network complexity increases, as more pore types are introduced into the sample. The PolyAmide (PA) matrix has an average void content of 6%, consisting of interbead channels with strong anisotropy. Alternating a carbon fibre layer with two polyamide layers slightly increases porosity (6.8% on average), as both inter- and intrabundle porosities are now present. It was found that the premature cutting of the carbon fibre bundle results in a large void at the end of the print path, while the start of the path is also associated with voids and an interruption of the PA wall layers. Full carbon fibre layering sections introduce additional large voids (average porosity of 9.7%), as the carbon fibre bundle cannot fully move into the corners of the polyamide wall layers.

The tested samples exhibit a delamination failure mode in the performed indentation test. The 100°PA<sub>2</sub>CF lay-up exhibits the best performance, yielding the highest loading and actuation potential. The presence of a PA layer between CF layers is beneficial for the mechanical performance of the printed carbon fibre composite. While reinforcements are introduced to enhance the mechanical strength and elasticity of thermoplastics, or to invoke an actuation mechanism, the final material properties strongly depend on the used fill pattern, the location of the start and end points of the print pattern, the turn radius, the lay-up, and more specifically the number of consecutive reinforcement layers.

**Keywords:** X-ray CT, defect detection, 3D printed carbon fibre reinforced plastics

## 1 Introduction

Several non-destructive methods and destructive methods for defect detection and product quality control. Industrial X-ray Computed Tomography (X-ray CT) has seen rapid improvements in recent years. With the acquisition time going down significantly and the constant improvement of image processing tools and resolution, X-ray CT has emerged as a viable option for inspection and quality control of (newly) engineered materials. In this study, X-ray CT is applied as an ‘manufacturing defects’ examination tool on 3D printed Carbon Fibre Reinforced Plastics (CFRPs). The repertoire of shapes that can be fabricated by industrial technologies is finite. 3D printing has the ability to remove this barrier, as it opens up vast new design spaces, allows for sophisticated microstructures, and therefore more intelligent composite structures.

CFRPs are increasingly being employed in diverse industries, among which primarily automotive and aerospace [1, 2]. Most 3D printed composites, however, still fail to mechanically compete with fibre reinforced composites produced by conventional manufacturing methods, such as autoclave curing or resin transfer moulding [3]. The manufactured 3D printed composites implement continuous carbon fibres, the primary load-carrying component in the composite, aiming for substantial mechanical improvements compared to 3D printed composites with discontinuous fibres [4 –7]. The CFRPs in this study were specifically designed to create internal actuation mechanisms. The design freedom provided by the additive manufacturing strategy was exploited to create an intelligent layered structure consisting of compliant and stiff materials. In this particular case, the mechanically induced actuation was achieved through a structure with alternating stiff Carbon Fibre (CF)/ PolyAmide (PA) composite layers and compliant pure PA layers.

Research on 3D printed CFRP structures is scarce and the current work aims to expand the knowledge concerning manufacturing defects in these composites. The presence of voids is inherent to additive manufacturing methods. The pore network within the pure matrix material layers has been reported to consist of interbead pores, while intrabead pores are absent. Adding a carbon fibre reinforcement phase significantly changes the microstructure of the composite and introduces intrabead pores in addition to the interbead pores [8 –11]. The size and origin of manufacturing defects associated with the chosen CFRP design and their influence on material properties is not well known. As a consequence, a 3D characterization of the microstructure is needed. X-ray CT allows defect detection, the quantification of void volume fractions and analysis of the orientation of pores and reinforcements in function of the chosen sample lay-up. The detailed microstructural characterization will provide a better understanding on the origin of defects, their influence on mechanical properties, and it will stimulate more intelligent part design of CFRPs with continuous fibres.



## 2 Materials and methods

### 2.1 Sample design

A Markforged MarkTwo desktop 3D printer is used to manufacture the continuous fibre reinforced composites. This desktop Fused Deposition Modelling (FDM) printer (see figure 1) utilizes two separate nozzles to supply the thermoplastic matrix material and the pre-impregnated continuous fibres. The pre-impregnation of the continuous fibre limits the possible material combinations. In this study, PA filaments were combined with PA pre-impregnated carbon fibres. Samples with variable CF reinforcement content were manufactured to study its influence on the mechanical properties of the composite (see section 2.3). In addition, one sample with four different layering sections was specifically manufactured for X-ray CT analysis, allowing to study the effect of the chosen lay-up on the presence of internal defects. This 10 x 10 x 20 mm X-ray CT sample consists of (1) a top section of concentric fill prepreg CF layers (see figure 2A, 2B), (2) two sections of pure  $\pm 45^\circ$  Road fill PA layers (see figure 2A, 2C, 2D), and (3) a section, with an alternating set of a concentric fill prepreg CF layer, followed by two road fill PA layers (CF + 2PA, see figure 2A).

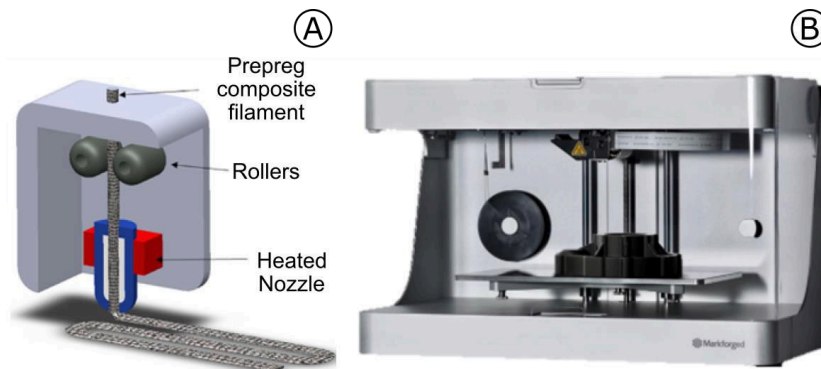


Figure 1: (A) Schematic representation of the 3D printing of a pre-impregnated continuous fibre, and (B) A Markforged desktop 3D printer model "MarkTwo" capable of printing continuous fibres [12, 13].

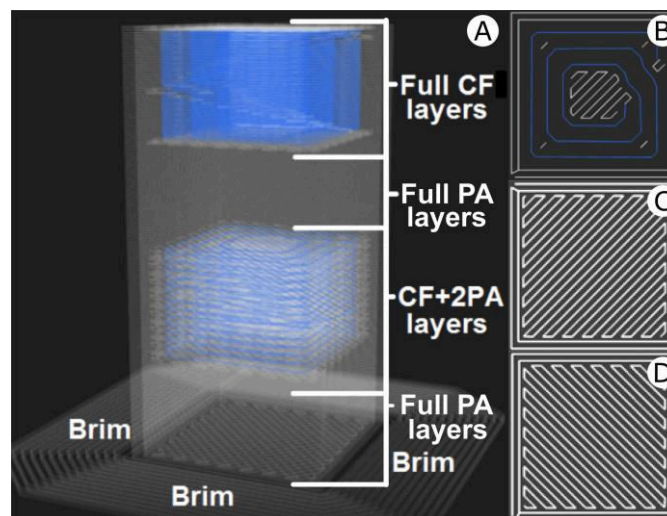


Figure 2: Schematic representation of the X-ray CT CFRP sample and its print patterns. (A) Layer-type regions of the sample. (B) Programmed concentric print pattern, with CF bundles in blue and PA layers in white. (C, D)  $\pm 45^\circ$  PA road fill print pattern.

### 2.2 X-ray computed Tomography

X-ray CT provides the means to acquire 3D digital models of samples in a non-destructive way, visualizing both the material composition and its internal architecture at the microscopic level [14–16]. Scans were performed on a Phoenix Nanotom S 180 kV  $\mu$ CT system from General Electric. The sample configuration allows examining material defects as a function of the chosen lay-up. A molybdenum target was installed during the scans, in nanofocus mode 0, and no additional filter materials were used. The X-ray tube voltage for the scan was set to 50 kV and the current to 400  $\mu$ A. A scan time of 20 minutes was achieved in the fast scan mode, in which frame averaging and image skip are disabled. During one scan, 2400 radiographic projections were taken over a 360° rotation. The exposure time was set to 500 ms, and an isotropic voxel size of 6 x 6 x 6  $\mu$ m was achieved. The Phoenix datoslx software was used to reconstruct the X-ray CT scans and to export cross-sectional images. The data was further processed using the 2D/3D image analysis software Avizo (v9.5), VoxTex (1.16c) and Matlab (R2016a).

In a first step the voids were separated from the carbon fibres and PA matrix. A dual threshold hysteresis function [17] was used, which returns a binary version of the original gray-scale image, based on two predefined thresholds (a weak one,  $T_w$  and a strong one,  $T_s$ ). Gray values in the histogram below  $T_w$  were labeled void in the binary image, while those above  $T_s$  were labeled as material. Subsequently, gray values that fall in between  $T_w$  and  $T_s$  were labeled as void or material, depending on their 4-way connectivity to labeled areas in the binary image. After this binarisation step, the total porosity of the geometric model and the porosity change as a function of the different layering types was calculated based on the marching cubes volume model [18] in 2D/3D image analysis software.

Three regions of interest representing the different layering sections, i.e., the PA-ROI, CF-ROI and CF+2PA-ROI, were selected and imported into VoxTex to convert the datasets into 8-bit voxel models. The latter are a discretization of the problem domain, generated using a regular rectangular mesh. The voxel model was generated by setting the mesh density to 12 pixels where the size of each pixel is 6  $\mu\text{m}$ . Thus, a single element in a voxel model is 72 x 72 x 72  $\mu\text{m}$  and each model contains more than 400 000 voxels. The structure tensor of the image was used to assign local orientation information to the elements in the voxel model. The decomposition of the structure tensor into eigenvalues,  $\lambda_1 \leq \lambda_2 \leq \lambda_3$ , and their associated eigenvectors, allows to define the structural anisotropy as  $A = 1 - \lambda_1/\lambda_3$ . The followed procedure for generating voxel models and calculating anisotropy is described in detail in [19, 20]. The orientation vectors of the voxels were defined in a Cartesian coordinate system, where the XY-plane represents the horizontal printing plane and the Z-axis denotes the stacking direction. The vector orientation angles were defined in a spherical coordinate system. The term “in-plane angle ( $\varphi$ )” defines the angle with the X-axis, in the printing plane, while the term “out-of-plane angle ( $\theta$ )” defines the angle with the vertical Z-axis. Cross-section images and 3D volume renderings of the pore network were generated in Avizo.

### 2.3 Mechanical testing

A displacement controlled indentation test, providing a local compressive load, was used to examine the internal actuation mechanism of the CFRPs. The indentation tests were performed on an Instron 5567 with a 30kN load-cell and a mounted 10 mm radius indenter. The tested samples were printed under an angle of  $10^\circ$  with respect to the Z-axis (see figure 3A), which resulted in a  $100^\circ$  angle between the horizontal surface of the mechanical test setup and the plies of the sample (see figure 3B). Four  $100^\circ$  sample types of varying CF content were tested. The CF content was altered by changing the amount of PA layers in the sample lay-up: (1) Full CF samples ( $100^\circ\text{PA}_0\text{CF}$ ), (2) samples with alternating 2 PA layers and 1 CF layer ( $100^\circ\text{PA}_2\text{CF}$ ), (3) samples with alternating 5 PA layers and 1 CF layer ( $100^\circ\text{PA}_5\text{CF}$ ) and (4) samples with alternating 10 PA layers and 1 CF layer ( $100^\circ\text{PA}_{10}\text{CF}$ ). Three samples were tested per lay-up type. Each sample is locally loaded at a position equal to 25% of its length with a fixed indentation speed of 0.5 mm/min. Limes cameras were used to monitor the indentation test. The images were processed with Vic-2D 2009 Digital Image Correlation (DIC) software by correlated solutions. Based on gathered DIC data, the out-of-plane rotational actuation angle at a specific load and indentation are quantified.

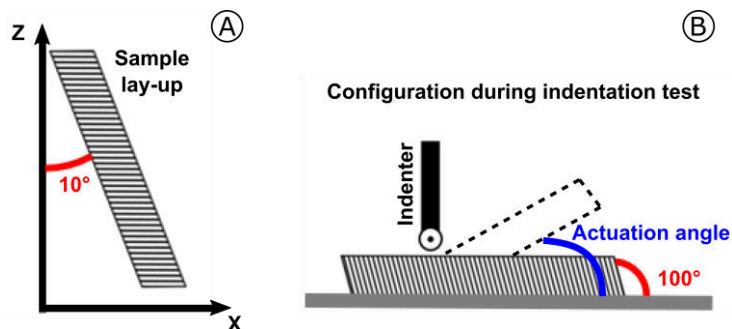


Figure 3: (A) Illustration of the  $10^\circ$  print angle with respect to the Z-axis and (B) the resulting  $100^\circ$  angle between the horizontal surface of the mechanical test setup and the printing plane. The out-of-plane rotational actuation angle is also indicated.

## 3 Results

### 3.1 Micro-structure characterization

The acquired X-ray CT geometrical models provide useful insight into the microstructure of the CFRP composites (see figure 4 and figure 5). First, the XY cross-sections through the pure PA layers show that the pore network consists of interbead channel porosity and that intrabead pores are absent (see figure 4A). Second, the XY cross-sections through the prepreg CF layers (see figure 4B) show the presence of voids near the start and end of the CF print pattern (green arrows) and in the corners, between the continuous CF bundles and the surrounding PA wall layers (red arrows). Third, it should be noted that the PA wall layers are discontinued at the start of the CF print pattern. Furthermore, voids occur in between and inside the CF bundles (blue and orange arrows, respectively). The intrabead pores most commonly occur along the outer shell of the concentric print pattern. Finally, it can be observed that twisting of the fibre bundle occurs at several locations.



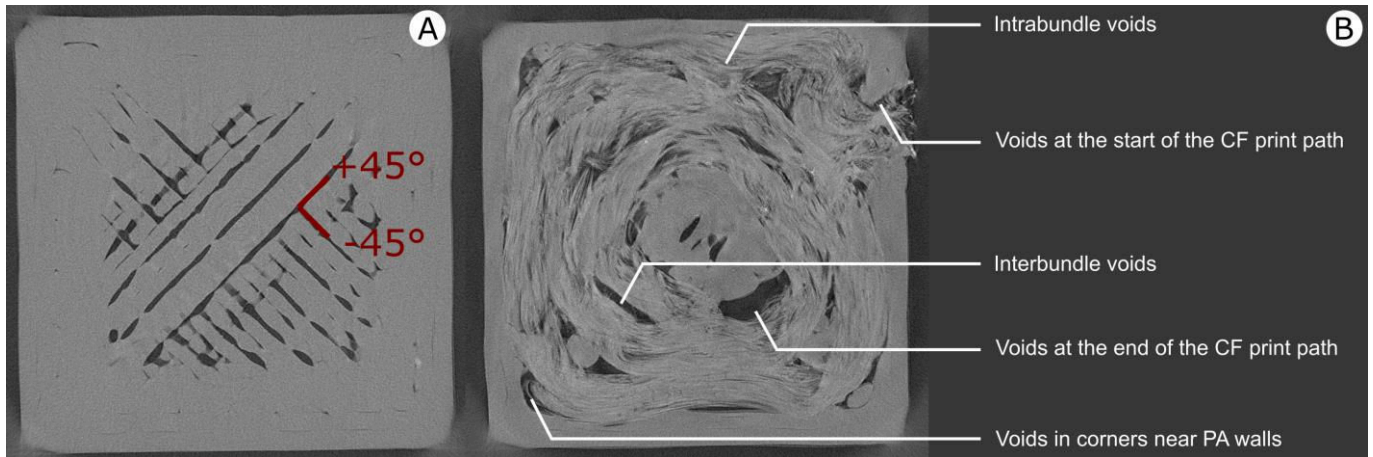


Figure 4: Cross-section images through the layering sections. (A) Horizontal cross-section through the full PA layers, showing the  $\pm 45^\circ$  interbead pore channels. (B) Horizontal cross-section through the full CF layering section, showing voids at the start and end of the print path, in the corners near PA walls, as well as inter- and intrabundle pores.

The 3D rendering of the X-ray CT CFRP sample highlights the differences between the layering sections (see figure 5A). In the pore network of the pure PA sections (PA-ROI), an inner interconnected interbead channel network, and an outer isolated interbead void network can be distinguished (see figure 5B). The regular stacking pattern of beads in the inner part of the full PA section results in a well-organized interbead channel structure. The voids in the outer part are interbead pores that either occur at the transition to the PA wall or in between the individual PA wall layers.

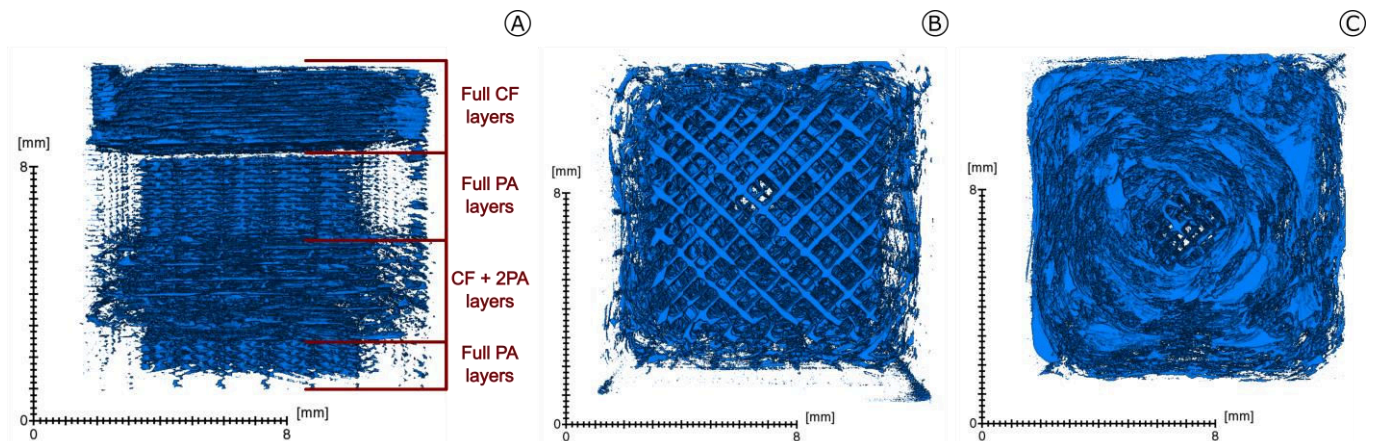


Figure 5: 3D rendering of the voids present in the 3D printed carbon fibre reinforced composite. (A) Front view on the composite sample, with the different layering sections indicated. (B) Bottom view on the composite sample, showing the voids in the full PA layering section. (C) top view of the composite sample, showing the voids in the full CF layering section.

The anisotropy and density histogram of the PA-ROI (see figure 6A) shows the presence of the PA matrix and voids. The PA matrix has a higher density compared to the voids, but generally plots at lower anisotropy compared to the interbead channel pores. To determine the interbead channel orientations in VoxTex, the density and anisotropy values of the PA matrix need to be eliminated. The latter was achieved by assigning threshold values for anisotropy (0.5) and density (170) during the orientation analysis. The orientation histograms of the interbead channels are computed based on the voxel model by considering only those elements with density  $< 170$  and anisotropy  $> 0.65$ . The orientation vectors of the interbead channels (see figure 6B) in the generated voxel model cluster in the XY-plane ( $\theta = 90^\circ$ ), at in-plane angles ( $\varphi$ ) of  $\pm 45^\circ$ , which is consistent with the applied  $\pm 45^\circ$  road fill print pattern for the PA beads.

In the full CF layering section (see figure 5A and 5C), pores with more irregular shapes are observed. The CF reinforcements appear as an additional cluster in the density and anisotropy histogram of the CF-ROI (see figure 7A). The prepreg carbon fibres have a slightly higher density and anisotropy compared to the PA matrix, overlap between the clusters is, however, expected. To determine the CF reinforcement orientations, the density and anisotropy values of the PA matrix and voids need to be eliminated. The orientation histograms of the CF reinforcements are computed by considering only the elements of the voxel model with a density  $> 200$ . By applying this threshold, voxels containing CF reinforcements with a density  $< 200$  are eliminated, but it ensures that the calculations exclude PA matrix or void voxels. The orientation vectors of the CF reinforcements (see figure 7B) in the

CF-ROI, as designed, align with the applied concentric print pattern. The print pattern predominantly follows the rectangular outline of the PA wall layers. As a consequence, the orientation vectors in the CF-ROI cluster in the XY-plane ( $\theta = 90^\circ$ ), at in-plane angles ( $\varphi$ ) of  $0^\circ$  and  $\pm 90^\circ$ . Scatter towards intermediate in-plane angles is observed.

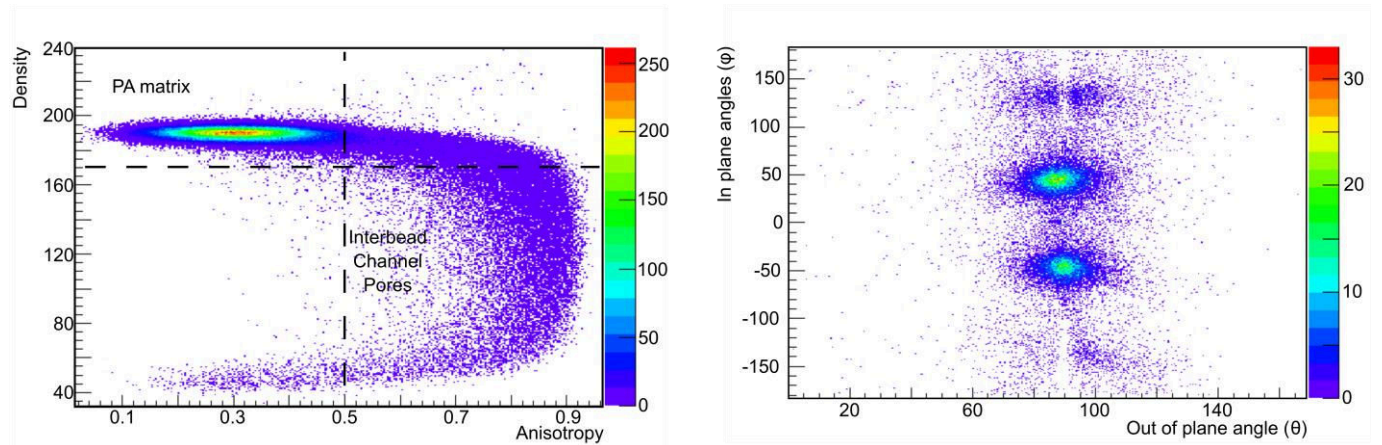


Figure 6: PA-ROI histograms. (A) Anisotropy – density histogram with the indicated thresholds for density (170) and anisotropy (0.5) that allow to separate between elements in the voxel model containing PA matrix and those containing interbead channel voids. (B) Orientation histogram of the interbead channel pores.

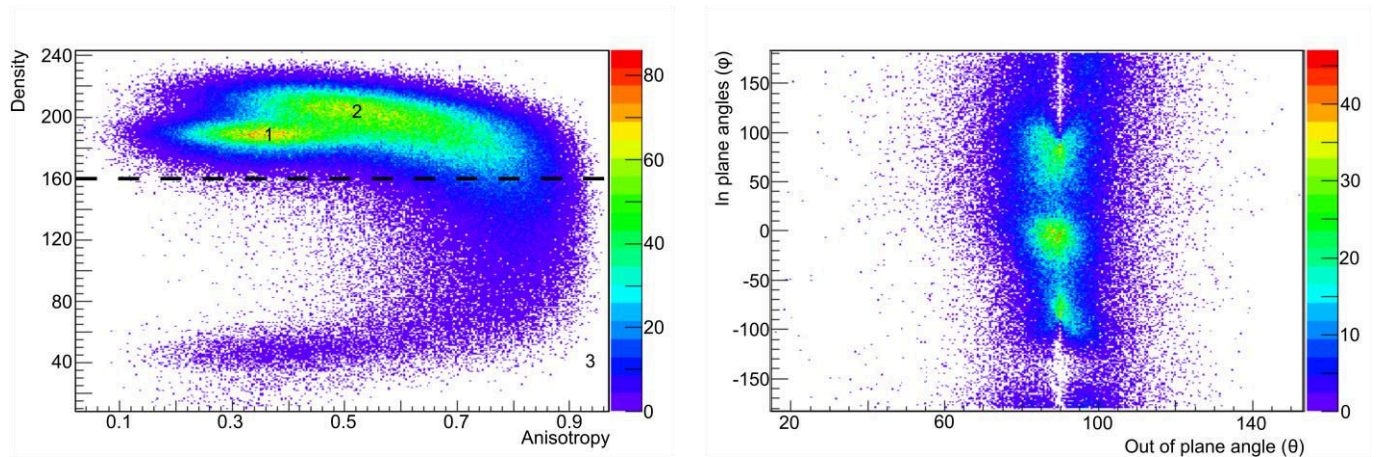


Figure 7: CF-ROI histograms. (A) Anisotropy – density histogram with three clusters indicated: (1) PA matrix cluster, (2) CF reinforcement cluster and (3) void cluster. Elements in the voxel model that represent voids plot at densities  $< 160$ . The CF reinforcements plot at higher anisotropy and density than the PA matrix. (B) Orientation histogram of the CF reinforcements.

Based on the three clusters that were observed in the generated density and anisotropy histograms, the voxel model of the CF-ROI can be segmented into a three phase model (see figure 8) based on a K-means clustering, containing respectively voids (white), PA matrix (transparent grey) and concentric CF reinforcements (blue). The model shows the general outline of the printed sample, but the level of detail is limited. CF reinforcements are, for example, discontinuous at certain locations in the model, whereas CT sections learn that they should be continuous.

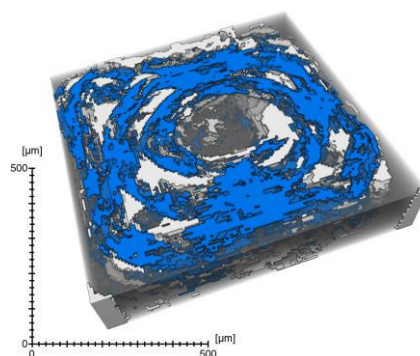


Figure 8: CF-ROI three phase model with voids (white), PA matrix (transparent grey) and CF concentric reinforcements (blue).



### 3.2 Void content analysis

The void content of the geometric model was quantified in each horizontal XY cross-section of the image stack and plotted with respect to their (vertical) Z-axis coordinates (see figure 9A). Porosity varies between 5% and 12% in the XY cross-sections, resulting in an average sample void volume fraction of 6.7%, which is similar to reported porosities in literature [21 -23]. At two intervals along the Z-axis, the porosity drops drastically (to < 1%). A vertical cross-section through the 3D printed composite sample (see figure 9B) illustrates how this phenomenon in the X-ray CT sample takes place just below the onset of the CF + 2PA and full CF layering sections.

Klift et al. [22] and Zhuo et al. [3] stated that porosity increases as more subsequent CF layers are implemented. This observation is confirmed in the current study. The full CF layering section, which is the uppermost section of the studied sample, yields an overall increasing porosity trend towards the top, as more and more subsequent CF reinforcement layers are implemented (see figure 9A and 9B). The full PA section has an average void volume fraction of 6%. The introduction of a concentric fill CF layers, alternating with two PA layers results in a more complex pore network compared to the full PA interbead channel pore network, but induces only in a slight increase in porosity (6.8% on average). In the full CF layering section porosity increases up to 9.7% on average.

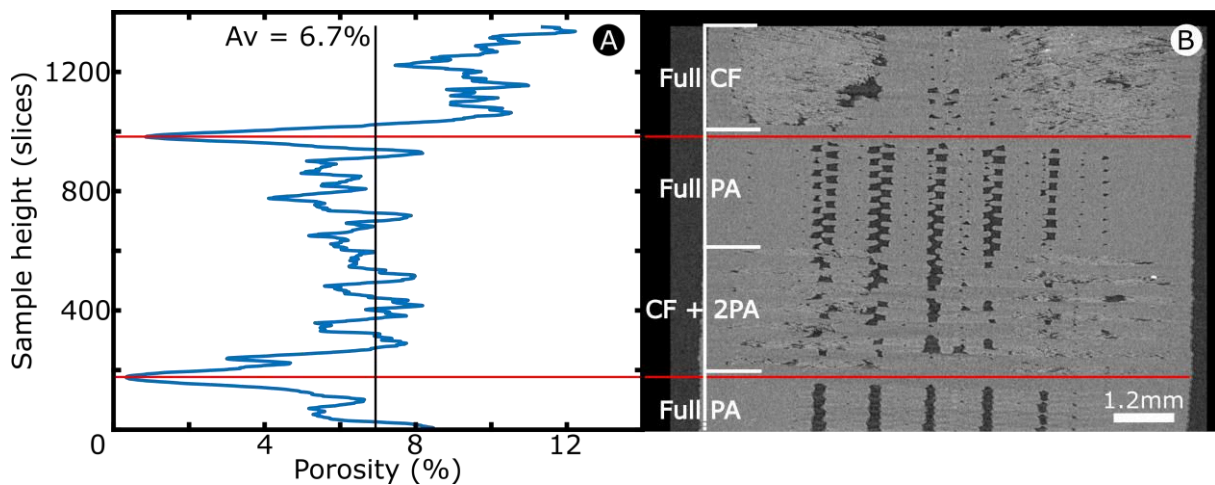


Figure 9: Void content analysis. (A) Porosity plotted versus sample height. The average void content is indicated with a black line. Red lines indicate local minima in porosity and their corresponding location in a vertical cross-section (B) through the 3D printed carbon fibre composite.

### 3.3 Mechanical testing

In this section, the indentation test results for the samples with a  $100^\circ$  angle between the XY-plane in the mechanical test setup and the plies are summarised. In contrast to the plastic deformation in full PA samples, the incorporation of CF reinforcements results in crack formation and ultimately failure, because of which equally high loading cannot be obtained. The CF reinforcements at the same time amplify the mechanically induced actuation potential of the sample. The average maximum load varies from 3260N to 3870N (cf. table 1).

Table 1 : Indentation result statistics for  $100^\circ$  samples, based on 3 test samples per group.

Sample	Vf (%)	Max load (N)	Max angle ( $^\circ$ )	Load (N) at crack initiation	Angle ( $^\circ$ ) at crack initiation
$100^\circ\text{PA}_0\text{CF}$	28.8	$3260\pm 60$	$45\pm 0.50$	$3060\pm 100$	$2.1\pm 0.43$
$100^\circ\text{PA}_2\text{CF}$	9.6	$3870\pm 160$	$49\pm 7.70$	$3570\pm 390$	$5.3\pm 2.70$
$100^\circ\text{PA}_5\text{CF}$	4.5	$3630\pm 60$	$29\pm 1.00$	$3460\pm 120$	$1.5\pm 0.49$
$100^\circ\text{PA}_{10}\text{CF}$	2.6	$3550\pm 100$	$32\pm 2.70$	$3390\pm 130$	$1.7\pm 0.48$

The  $100^\circ\text{PA}_2\text{CF}$  lay-up exhibits the highest ultimate strength and actuation potential and crack initiation occurs at a higher load compared to the other sample types. The obtained actuation angle for the  $100^\circ\text{PA}_2\text{CF}$  lay-up at crack initiation is two times larger than for the other sample types. The variation on this angle is, however, larger which implicates a lower consistency. In contrast to the  $100^\circ\text{PA}_2\text{CF}$  lay-up, the full CF samples ( $100^\circ\text{PA}_0\text{CF}$ ) yield overall low load values while maintaining reasonable high actuation angles. In general, the investigated CFRPs exhibit a delamination failure mode. The indentation force triggers the buckling of the stiff phases, and as a result, the adjacent matrix starts to tear. Matrix tearing was observed to occur at the interlaminar interface, which complies with the anisotropic characteristics of the material, and are inherent to a sample design with alternating PA and concentric CF plies.

## 4 Discussion and conclusion

X-ray CT imaging of a 3D printed composite provides useful insight into its microstructure. Interbead channels within PA layers occur due to insufficient packing of adjacent extrusion roads. Voids near the end of the CF print pattern indicate that the CF bundle is cut before fully completing its programmed print path. Intrabundle pores in the CF sections are likely a consequence of fibre bundles being pushed and draped over the substrate, especially near the start of the print pattern. The latter process induces buckling of the CF bundles, which causes them to open up. Strategically locating the start and end point of the print pattern might influence the final mechanical behavior of the composite. Some matrix fill parts were presumably programmed too small to be recognized by the printing software. Adequate path configurations should be used to avoid the inherent creation of interbundle voids. Twisting and buckling of the CF bundles in the concentric fill pattern might be reduced if larger turn radii are used.

The two local porosity minima (< 1% porosity), in the porosity profiles in figure 9, are likely related to the position of the fibre nozzle, which is set at a lower height than the matrix nozzle. Consequently, the underlying PA layer is compacted and its void content reduced. A lay-up of one CF layer and two PA layers lowers the pore alignment, but does not drastically change the void content compared to the full PA layering sections. The amount of porosity increases with the amount of CF layers, as it introduces increasingly larger and irregularly shaped voids. The porosity measurements by X-ray CT are in good agreement with the porosity values that are found in the literature. The accuracy of X-ray CT porosity characterization will, however, depend on the voxel resolution and the error will rapidly increase for the evaluation of small defects [23], e.g., defects smaller than three times the voxel resolution, while even smaller voids will be absent in the X-ray CT acquisitions. X-ray CT has proven itself as an effective tool for geometrical characterization of internal defects in CFRPs. The obtained 3D information about internal voids extracted from X-ray CT datasets can be utilized in production processes optimization, in understanding the influence of defects on mechanical properties and in quality control.

The voxel model derived orientations of the interbead channel pores are in good agreement with the with the applied  $\pm 45^\circ$  road fill print pattern for the PA beads. The CF reinforcements are printed in a concentric print pattern and orientation analysis shows how the reinforcements dominantly follow the rectangular outline of the PA wall layers. The three phase finite element model shows the general outline of the actual sample geometry, but the model quality is insufficient to accurately simulate material properties, due to the limited phase-contrast between the PA matrix and CF reinforcements. Several steps can be taken to improve the model quality. One possibility is downsizing the printed composite sample, which will increase the voxel resolution of the X-ray CT scans and might allow scanning at lower X-ray energy, which in turn could improve the phase-contrast. Better phase-contrast can also be obtained by using glass fibre instead of carbon fibre as reinforcement material. It should, however, be considered that while changing the sample size and/or its components might improve the finite element model quality and might assist in defect detection, it will also change the mechanical behavior of the 3D printed sample.

The investigated CFRPs exhibit a delamination failure mode in the indentation test. The  $100^\circ\text{PA}_2\text{CF}$  lay-up exhibits the best performance. The higher actuation potential for this type of sample compared to the others is directly linked to its design and microstructure. In general, high CF content samples ( $100^\circ\text{PA}_0\text{CF}$  and  $100^\circ\text{PA}_2\text{CF}$ ) outperform the low CF content samples ( $100^\circ\text{PA}_5\text{CF}$  and  $100^\circ\text{PA}_{10}\text{CF}$ ). The latter do not achieve the same actuation angles, as they fail at smaller indentation depths. The ultimate strength and the actuation potential of the samples improves as the CF content increases. However, the sample type with the highest CF content ( $100^\circ\text{PA}_0\text{CF}$ ) yields overall low load values, while maintaining reasonably high actuation angles. The latter indicates that the presence of a PA layer between CF layers is beneficial. As the void content increases with an increasing number of consecutive CF layers, it is expected that the ultimate strength lowers from  $100^\circ\text{PA}_2\text{CF}$  to  $100^\circ\text{PA}_0\text{CF}$ . In the  $100^\circ\text{PA}_0\text{CF}$  lay-up there are no remaining PA layers in between the CF layers and as such, the fibre starting points, and the associated discontinuities in the PA wall layers, are in close proximity. These defects will, together with the increased void content, form stress concentration zones under the applied indentation force. As a consequence, cracks will initiate faster and grow rapidly at the bonding interface between CF layers. Even though the load stagnates at low values, the PA wall layers deform extensively before failure, explaining why reasonably high actuation angles can still be achieved.

The results demonstrate that, while reinforcements are introduced to enhance the mechanical strength and elasticity of thermoplastics, or to amplify an internal actuation mechanisms, the microstructure of the designed composite strongly depends on the used road fill, the start and end location of the print pattern, the turn radius, and the lay-up, with more specifically the number of consecutive reinforcement layers and PA layers. Future research should point out to which extent additional changes in the design can influence the mechanical properties of printed composites. Application oriented evaluations should be performed to fine-tune the product design towards the desired structural and mechanical properties.

### Acknowledgements

The authors would like to acknowledge the KU Leuven project C24/17/052, regarding in situ X-ray CT characterization of composite materials and tissues during mechanical testing. This study was also made possible through a FWO large infrastructure project (I013518N): The KU Leuven X-ray computed tomography centre: a versatile and structured way to unravel the material structures and dynamic processes. Yentl Swolfs acknowledges FWO Flanders for his post-doctoral fellowship.

## References

- [1] S. Peters, G. Lanza, J. Ni, J. Xiaoning, Y. Pei-Yun, M. Colledani, Automotive manufacturing technologies, an international viewpoint, *Manufacturing Review* (2014) 1-10.
- [2] R. Bogue, 3d printing: the dawn of a new era in manufacturing?, *Assembly Automation* 33(4) (2013) 307–311.
- [3] P. Zhuo, S. Li, I. Ashcroft, A. Jones, X. Hou, J. Pu, 3D printing of continuous fibre reinforced thermoplastic composites, 21<sup>st</sup> International Conference on Composite Materials (2017) 20-25.
- [4] R. Matsuzaki, M. Ueda, M. Namiki, T. Jeong, H. Asahara, K. Horiguchi, T. Nakamura, A. Todoroki, Y. Hirano, Three-dimensional printing of continuous-fiber composites by in-nozzle impregnation, *Scientific reports* 6:23058 (2016).
- [5] C. Hsueh, Young's modulus of unidirectional discontinuous-fibre composites, *Composites Science and Technology* 60(14) (2000) 2671–2680.
- [6] C.L. Tucker III, E. Lian,. Stiffness predictions for unidirectional short-fiber composites: review and evaluation, *Composites science and technology* 59(5) (1999) 655–671.
- [7] P.J. Hine, H.R. Lusti, A.A. Gusev, Numerical simulation of the effects of volume fraction, aspect ratio and fibre length distribution on the elastic and thermoelastic properties of short fibre composites, *Composites science and technology* 62(10) (2002) 1445–1453.
- [8] H.L. Tekinalp, V. Kunc, G.M. Velez-Garcia, C.E Duty, L.J. Love, A.K. Naskar, C.A. Blue, S. Ozcan, Highly oriented carbon fiber–polymer composites via additive manufacturing, *Composites Science and Technology* 105 (2014) 144–150.
- [9] F. Ning, W. Cong, Y. Hu, and H. Wang, Additive manufacturing of carbon fiber-reinforced plastic composites using fused deposition modeling: Effects of process parameters on tensile properties, *Journal of Composite Materials* 51(4) (2017) 451–462.
- [10] W. Zhang, C. Cotton, J. Sun, D. Heider, B. Gu, B. Sun, .T. Chou, Interfacial bonding strength of short carbon fiber/acrylonitrile-butadiene-styrene composites fabricated by fused deposition modeling, *Composites Part B: Engineering* 137 (2018) 51–59.
- [11] S-Y. Fu, B. Lauke, E. Mäder, C-Y. Yue, and X. Hu, Tensile properties of short-glass-fiber-and short-carbon-fiber-reinforced polypropylene composites. *Composites Part A: Applied Science and Manufacturing* 31(10) (2000) 1117–1125.
- [12] Markforged 3D printers, <https://markforged.com/mark-two/>, 2018 (accessed on 14 October 2018).
- [13] G.D. Goh, V. Dikshit, A.P. Nagalingam, G.L. Goh, S. Agarwala, S.L. Sing, J. Wei, W.Y. Yeong. Characterization of mechanical properties and fracture mode of additively manufactured carbon fiber and glass fiber reinforced thermoplastics. *Materials & Design* 137 (2018) 79–89.
- [14] A.Y. Sasov, Microtomography 2. examples of applications, *Journal of Microscopy-Oxford* 147 (1987) 179-92.
- [15] L.A. Feldkamp, L.C. Davis, J.W. Kress, Practical cone-beam algorithm, *Journal of the Optical Society of America a-Optics Image Science and Vision* 1(6) (1984) 612–619.
- [16] M. Wevers, B. Nicolăi, P. Verboven, R. Swennen, S. Roels, E. Verstrynge, S.V. Lomov, G. Kerckhofs, B. Van Meerbeek, A.Mavridou, L. Bergmans, P. Lambrechts, J. Soete, S. Claes, H. Claes, Applications of CT for non-destructive testing and materials characterization, in: S. Carmignato, W. Dewulf, R. Leach (Eds.), *Industrial X-Ray Computed Tomography*, Springer, Switzerland, 2018, pp. 267–331.
- [17] J. Canny, A computational approach to edge detection, *Ieee Transactions on Pattern Analysis and Machine Intelligence* 8(6) (1986) 679-98.
- [18] W.E. Lorensen, H.E. Cline, Marching cubes: A high resolution 3D surface construction algorithm, *Siggraph Comput Graph.* 21(4) (1987) 163–9.
- [19] I. Straumit, S. V. Lomov, M. Wevers, Quantification of the internal structure and automatic generation of voxel models of textile composites from X-ray computed tomography data, *Composites: Part A* 69 (2015) 150–158.
- [20] N.Q.Nguyen, M. Mehdikhani, I. Straumit, L. Gorbatiikh, L. Lessard, S.V. Lomov, Micro-CT measurement of fibre misalignment: Application to carbon/epoxy laminates manufactured in autoclave and by vacuum assisted resin transfer moulding, *Composites: Part A* 104 (2018) 14–23.
- [21] C. Yang, X. Tian, T. Liu, Y. Cao, D. Li, 3D printing for continuous fiber reinforced thermoplastic composites: mechanism and performance, *Rapid Prototyping Journal* 23(1) (2017) 209–215.
- [22] J. Justo, L. Távara, L. García-Guzmán, F. París, Characterization of 3d printed long fibre reinforced composites, *Composite Structures* 185 (2018) 537–548.
- [22] F. Van Der Klift, Y. Koga, A. Todoroki, M. Ueda, Y. Hirano, R. Matsuzaki, 3D printing of continuous carbon fibre reinforced thermo-plastic (CFRTP) tensile test specimens, *Open Journal of Composite Materials* 6(01) (2016) 18–27.
- [23] P. Hermanek, S. Carmignato, Reference object for evaluating the accuracy of porosity measurements by X-ray computed tomography, *Case Studies in Nondestructive Testing and evaluation* 6 (2016) 122–127.